Journal of Materials Chemistry A

PAPER

View Article Online
View Journal | View Issue

Cite this: J. Mater. Chem. A, 2017, 5, 9262

Dichlorosilane-derived nano-silicon inside hollow carbon spheres as a high-performance anode for Li-ion batteries†

Tony Jaumann,[a] Maik Gerwig,[b] Juan Balach,[c] Steffen Oswald,[a] Erica Brendler,[b] Ralf Hauser,[d] Bernd Kieback,[d] Jürgen Eckert,[ef] Lars Giebeler *[a] and Edwin Kroke[b]

A novel and cost-effective synthesis of silicon nanocrystallites (<10 nm) sealed in hollow carbon spheres (nc-Si@HCS) is developed as a promising anode material for high-performance Li-ion batteries (LIBs). The preparation method involves dichlorosilane (H_2SiCl_2) as widely available feedstock, to form a hydrogen-rich polysiloxane as a precursor for the production of large quantities of silicon nanoparticles. The final electrode material is composed of agglomerated 5 nm sized silicon nanoparticles encapsulated within hollow micro-sized carbon structures. A high specific capacity of 1570 mA h $g_{electrode}^{-1}$ at 0.25 A g^{-1} with a capacity retention of 65% after 250 deep discharge cycles and a reversible high areal capacity of up to 4 mA h cm^{-2} at a total mass loading of 3.2 mg cm^{-2} impressively demonstrate the excellent features of this novel anode material. We performed a detailed structural as well as electrochemical characterization in different electrolytes. Post mortem investigations help to understand the degradation mechanism in our material. The study herein heralds a new approach to structurally design advanced negative electrode materials with the potential to increase the specific energy of LIBs and to boost future electro-mobility technology.

Received 6th January 2017
Accepted 27th March 2017

DOI: 10.1039/c7ta00188f

rsc.li/materials-a

Introduction

The worldwide utilization of green energy is one of the most urgent issues in the current century. The success of this complex project depends considerably on the development of efficient and low-cost energy storage systems with high power and energy density.[1] Electro-mobility will play a key role in efficiently exploiting green energy in order to not only reduce CO_2 emission by combustion engines, but also guarantee a safe and reliable power grid (vehicle-to-grid) supplied by regenerative energy. Li-ion batteries (LIBs), already installed in most portable electronic devices, are one of the most promising technologies for electro-mobility due to high energy density and excellent reversibility. In this regard, the first electric vehicles equipped with LIBs have found their way onto roads. However, the limited energy density and high production costs of LIBs are still major reasons for the low acceptance of electric vehicles by broad society. Therefore, the development of new and cheap electrode materials with higher capacity is inevitable.[2] Silicon is an attractive anode material for LIBs due to its extremely high theoretical capacity of 3600 mA h g^{-1}, up to 10 times higher than that of commonly used graphite (372 mA h g^{-1}) and wide availability.[3] It is expected to increase up to 40% the overall specific energy density of state-of-the-art LIBs from 250 W h kg^{-1} to 350 W h kg^{-1} at the cell level. However, during electrochemical lithiation of silicon the volume increases up to 300% causing drastic mechanical stress eventually resulting in crack propagation of individual particles. This mechanism causes a low cycle stability preventing broad commercialization. Silicon nanostructures[4] and amorphous structures[5] can overcome pulverization and enhance cycle life. The critical diameter of individual particles was found to be approximately 150 nm.[4] It was further observed that small-sized silicon nanoparticles (<20 nm) show even further enhanced reversibility due to a stabilized surface film.[6–8] Even though nanostructured silicon does not suffer from pulverization, capacity fading is typically still high due to contact loss from the conductive current collector.[9] Among the volume changes causing displacement of the particles, the origin of capacity fading is mostly attributed to

[a]Leibniz Institute for Solid State and Materials Research (IFW) Dresden e.V., Institute for Complex Materials, Helmholtzstraße 20, D-01069 Dresden, Germany. E-mail: l.giebeler@ifw-dresden.de; Fax: +49 351 4659 452; Tel: +49 351 4659 652

[b]Technische Universität Bergakademie Freiberg, Institut für Anorganische Chemie, Leipziger Straße 29, D-09596 Freiberg, Germany

[c]Department of Chemistry, Universidad Nacional de Río Cuarto-CONICET, Route 36 Km 601, X5804ZAB Río Cuarto, Argentina

[d]Fraunhofer Institute for Manufacturing Technology and Advanced Materials IFAM, Branch Lab Dresden, Winterbergstraße 28, D-01277 Dresden, Germany

[e]Austrian Academy of Sciences, Erich Schmid Institute of Materials Science, Jahnstraße 12, A-8700 Leoben, Austria

[f]Montanuniversität Leoben, Department Materials Physics, Jahnstraße 12, A-8700 Leoben, Austria

† Electronic supplementary information (ESI) available. See DOI: 10.1039/c7ta00188f

an instable solid electrolyte interface (SEI) which repeatedly grows during cycling and therewith consumes a larger amount of electrolyte as was demonstrated in many previous studies.[10–12] In order to prevent contact loss and to lower the SEI growth rate, hollow carbon spheres (HCSs) with embedded silicon nanoparticles turned out to be efficient structures as anode materials. The use of HCSs retains the electrical contact over cycling and may even work as a stable artificial SEI. The large volume change of silicon is effectively buffered by the void space inside the carbon sphere. These structures show greatly improved performance compared to conventional silicon nanoparticles and core–shell carbon-coated silicon nanoparticles.[13] Several synthesis approaches have been proposed to obtain such materials,[10,13,14] but most of them use commercially available, expensive silicon nanoparticles of 50 to 150 nm in size to design a hollow carbon sphere around these particles. However, these synthesis strategies are quite complex and seem to be not viable for mass production. Furthermore, these silicon particles may suffer from pulverization since their size is close to the critical crack length. Recently, the material class hydrogen silsesquioxane (HSQ), a polysiloxane with the chemical formula $(HSiO_{1.5})_n$, has gained considerable attention for the preparation of nanostructured silicon anodes for secondary lithium batteries.[7,15–17] HSQ is commercially available and can be easily produced through hydrolysis of widely available and low-cost silanes such as triethoxysilane and trichlorosilane.[7,18,19] Thermal processing of the polysiloxane initiates a complex decomposition and transformation to silicon nanoparticles and silicon dioxide, similar to the disproportion of silicon monoxide which is another interesting material class for the synthesis of hollow nanostructured silicon anodes.[20] Pauthe *et al.* first reported about silicon formation by annealing of HSQ at temperatures over 500 °C.[21] Hessel *et al.* further successfully demonstrated the preparation of individual silicon nanoparticles.[18] Recently, we used trichlorosilane as a suitable and economic HSQ precursor to prepare silicon nanoparticles embedded within porous and hollow carbon structures.[16] While the silica matrix itself serves as a template for the carbon, the active silicon nanoparticles are liberated by HF etching from the silica. However, the quantity of silicon within the annealed HSQ is low and accounts to a maximum of 13 wt% since the mass of silicon correlates with the hydrogen concentration in HSQ.[18] Increasing the number of Si–H bonds in the structure of the polysiloxane will result in more silicon nanoparticles within in the silica matrix, higher capacity of the final anode material and lower production costs.

In the present work, we provide a new and easily scalable preparation method for large amounts of 5 nm sized silicon nanocrystallites tightly embedded within micrometer-sized hollow carbon spheres (nc-Si@HCS). The silicon–carbon nanocomposite is derived from hydrolyzed dichlorosilane (HDCS), a low-cost polysiloxane containing a high concentration of H–Si and H_2Si moieties. Annealing at a high temperature of 1150 °C and a fast heating rate (50 K min^{-1}) cause a transformation to about 15–17 wt% of silicon nanoparticles embedded in silica which is up to 35% higher than that theoretically possible for HSQ. It will be shown that the small particle size of the obtained silicon and the design of the carbon scaffold are excellent preconditions for application as a high-performance anode material for LIBs. Different electrolytes suitable for LIBs were used to provide a better comparison with literature data. Finally, the material was examined after cycling in order to understand the outperforming electrochemical behavior.

Results and discussion

Characterization of the HDCS precursor

FT-IR and NMR spectroscopy were carried out for the as-synthesized HDCS, in order to verify the successful formation of the essential Si–H bonds within the polysiloxane and to test the stability under ambient conditions. In addition, a conventional HSQ precursor was prepared by solvent-free hydrolysis of trichlorosilane (HTCS).[19,22] The IR spectra of both compounds are presented in Fig. 1a. For HDCS, we observe intense Si–H stretching absorption bands at 2180 and 2250 cm^{-1}, the Si–O–Si vibration at 1000–1200 cm^{-1}, the H–Si–H vibration at 900–1000 cm^{-1} and the H–Si–O vibration at 820 cm^{-1}.[23] These functional groups are very typical of HDCS with the formula $(H_2SiO)_n$.[23] Its stability in air is verified by an additional spectrum after storage under ambient conditions for three months. In contrast, the

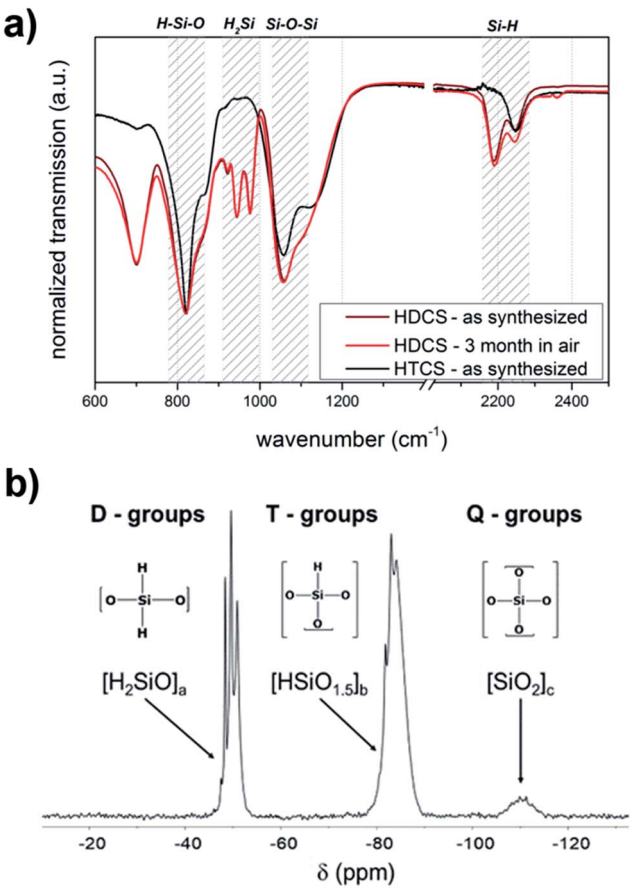

Fig. 1 (a) The FTIR spectra of the HDCS and HTCS precursors before and after storage in air for three months, and (b) the ^{29}Si MAS NMR spectrum of the as-synthesized HDCS precursor.

HTCS shows now absorption bands within the region of 900–1000 cm^{-1} and less intense Si–H stretching at 2250 cm^{-1}. This result suggests a chemical formula of $(HSiO_{1.5})_n$ as proposed by other groups.[19] Detailed information about the molecular structure of HDCS is obtained using ^{29}Si solid state NMR spectroscopy. The spectrum (Fig. 1b) shows three signal groups at −47.0 to −53.0, −79.0 to −88.0 and −105.0 to −115.0 ppm, which are characteristic of, respectively, D-groups ($[H_2SiO]$),[23,24] T-groups ($[HSiO_{1.5}]$)[25] and Q-groups ($[SiO_2]$)[26] in hydrogen terminated oligosiloxanes. In particular, the signals of D- and T-groups split into several peaks and shoulders. Previous ^{29}Si NMR investigations on siloxanes have shown that the chemical shift depends not only on the direct substituents but also on the neighboring units in the siloxane network.[27] In this regard, for example, one D-group connected with two other D groups results in a higher chemical shift of the ^{29}Si NMR signal than a moiety connected with two T-groups. The signal splitting shows that the different units are all present in the polymeric network. A quantitative analysis of the structural units based on ^{29}Si NMR resulted in 33% D-, 62% T- and 5% Q-groups providing a composition for the polysiloxane of $([H_2SiO]_1[HSiO_{1.5}]_{1.9}[SiO_2]_{0.15})_n$. In addition to the D-groups formed by the hydrolysis of dichlorosilane as expected according to eqn (1) the material consists of a large part of T-groups.

$$n H_2SiCl_2 + n H_2O \rightarrow (H_2SiO)_n + n HCl \quad (1)$$

Hydrogen chloride which is formed as a byproduct can induce the formation of new Si–Cl bonds from the existing Si–H bonds according to eqn (2).[23] After hydrolysis of the new Si–Cl bonds, the observed highly branched siloxane units can be formed.

$$Si–H + HCl \rightarrow Si–Cl + H_2 \quad (2)$$

Another reason for the formation of T-units from dichlorosilane (DCS) may be Lewis-base catalyzed dismutation, yielding monochlorosilane (M-units), trichlorosilane (TCS, T-units) and silicon tetrachloride (STC, Q-units) according to eqn (3) and (4). Amine-induced dismutation of DCS and trichlorosilane is well known.[28,29] Hydrolysis of these chlorosilanes leads to the observed D-, T- and Q-groups. Due to the volatility of monochlorosilane (and monosilane, SiH_4, which might also be formed) M-units are not detectable in the ^{29}Si MAS NMR spectra.

$$2H_2SiCl_2 \rightarrow H_3SiCl + HSiCl_3 \quad (3)$$

$$2HSiCl_3 \rightarrow H_2SiCl_2 + SiCl_4 \quad (4)$$

These results clearly demonstrate the successful formation of a hydrogen-rich polysiloxane by hydrolysis of dichlorosilane *via* a very facile synthesis involving low cost chemicals.

Characterization of the annealed HDCS

It is well accepted that HSQ decomposes and transforms into a silica matrix with embedded silicon nanoparticles in a temperature range of 300–1000 °C. In the case of a HSQ (here HTCS) which mainly contains T-groups ($HSiO_{1.5}$), the reaction is supposed to go along the following simplified equation (eqn (5)):[18]

$$4(HSiO_{1.5})_n \xrightarrow{350–450\ ^\circ C} n\ SiH_4 + 3n\ SiO_2 \xrightarrow{T > 450\ ^\circ C} n Si + 2n H_2 + 3n SiO_2 \quad (5)$$

Hence, the quantity of Si–H bonds is essential for the successful synthesis of the final nanostructured silicon. Based on eqn (5), the maximum quantity of silicon within the silica matrix is determined to be 13 wt% at most. Thermal decomposition of the D-groups (H_2SiO), which are present in high quantities in the HDCS, is expected to be similar and is expressed by simplified eqn (6).

$$(H_2SiO)_n \xrightarrow{250–450\ ^\circ C} \frac{n}{2} SiH_4 + \frac{n}{2} SiO_2 \quad (6)$$

The thermal processing is followed by a complex redistribution of the polysiloxane cage network to SiO_x species accompanied by the loss of monosilane which may start at temperatures slightly lower than those observed for HSQ due to the more prone H_2SiO groups. The monosilane further decomposes into silicon and hydrogen ((eqn (7)) at about 450 °C.

$$SiH_4 \xrightarrow{over\ 450\ ^\circ C} Si + 2H_2 \quad (7)$$

Considering the determined composition of $([H_2SiO]_1[HSiO_{1.5}]_{1.9}[SiO_2]_{0.15})_n$ for the HDCS, a theoretical silicon concentration of 17.6 wt% is possible which is 35% higher than for conventional HSQ consisting mostly of T-groups. Note that even higher silicon concentrations can be achieved by incorporating more D-groups within the polysiloxane. A notable issue is the diffusion of silane out of the silica matrix reducing the yield of silicon within the silica matrix. Among other strategies one strategy to minimize loss of silicon is use of a fast heating rate,[18] in order to decompose immediately the *in situ* formed silane. Although we used a relatively high heating rate of 50 K min^{-1}, silane still seems to evaporate and deposit on the hot reactor wall visible as a brownish coating (Fig. S1a and b†). The deposit was analyzed by SEM coupled with EDXS (Fig. S1c and d†) clearly showing silicon nanoparticles of 50–100 nm in the graphite oven. The loss of silane was reduced by placing the HDCS in a graphite crucible instead of a corundum one which seems to enhance the thermal conductivity and induces a fast transformation. Hessel *et al.* also suggested using an argon/hydrogen atmosphere in order to minimize the escape of monosilane which may be a strategy for future work to increase the amount of silicon within the annealed HDCS.[18] Using a graphite crucible, the total weight loss was reduced to about 5 wt% mainly due to hydrogen loss, accounting to a theoretical silicon concentration of 15.4 wt% within the composite based on the composition of $([H_2SiO]_1[HSiO_{1.5}]_{1.9}[SiO_2]_{0.15})_n$ and eqn (6) and (7). The silicon concentration of the composite was analyzed by EDX, NMR and XP spectroscopy and compared to the results with the reference sample HTCS (Table 1).

EDXS was used to determine the oxygen and the silicon concentration at four different spots. Taking the average (Fig. S2†) and assuming that oxygen is only bonded to silicon in the form of SiO_2, a silicon concentration of 14 and 21 wt% was calculated for, respectively, HTCS and HDCS. These values are 10–35% higher than the theoretical considerations and therewith likely overvalued, partially related to the low accuracy of EDXS for elements of low atomic numbers. Hence, we further carried out ^{29}Si MAS NMR spectroscopy (Fig. 2a) which reveals in both cases two separated signals at −80 ppm and −110 ppm corresponding to Si(0) and Si(+4), respectively. The Si(0) signal is additionally composed of three overlapped peaks due to the presence of amorphous and crystalline silicon with different sizes. A peak deconvolution resulted in 9 wt% Si for HTCS and 10.4 wt% Si for HDCS which are lower than expected. The reason may be found in the poor resolution due to the long relaxation time of silicon[21] and the large peak broadening of amorphous silicon as well as small silicon clusters causing a low signal to noise ratio.

However, the results confirm a higher silicon composition in the annealed HDCS. Taking the average of both techniques (EDXS and NMR), the theoretically calculated silicon composition within both annealed polysiloxanes can be confirmed. In addition, XPS was carried out (Fig. 2b) which is a powerful tool to analyze the binding energies of an element and the surface characteristics. In both cases, low concentrations of silicon can be identified at about 99 eV and large quantities of silica at about 104 eV. The deconvolution of the Si 2p level resulted in about 6 wt% silicon for both cases indicating that most silicon is located in the core of the composite and therewith cannot be detected by XPS. The overall results indicate that the silicon concentration is about 30% higher in the HDCS than in the conventional HTCS.

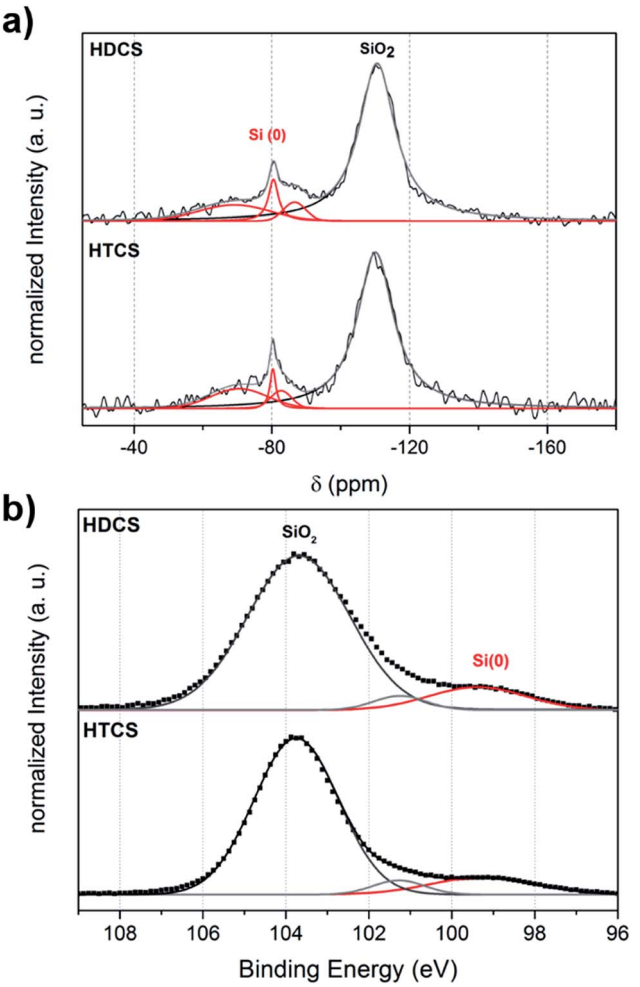

Fig. 2 (a) ^{29}Si MAS NMR spectra and (b) Si 2p XP spectra of the annealed HDCS and HTCS.

Structural characterization of the nc-Si@HCS

We characterized the final nc-Si@HCS composite derived from HDCS by electron microscopy, as schematically represented in Fig. 3a. A representative SEM image of the annealed HDCS at low magnification is shown in Fig. S3a.† We can mostly observe agglomerated spheres of sizes between 0.3 and 2 μm and some unspecific structures. In Fig. S3b,† a representative SEM image of the formed nc-Si@HCS simply synthesized by coating of the annealed HDCS with sucrose, carbonization and etching in diluted HF in order to remove the inactive SiO_2 is shown. Subsequently closely packed half-open and retained spheres of 0.3–2 μm in diameter are obtained. Also some unspecific micrometer-sized carbon structures are present as a result of the inhomogeneous HDCS precursor. These results indicate that the annealed HDCS precursor serves as a good template to replicate hollow carbon structures. EDX spectroscopy (Fig. S4†) of the nc-Si@HCS proves the presence of predominantly silicon and carbon. We determined a silicon concentration of about 49 wt%. The silicon content was additionally verified by thermogravimetric combustion in synthetic air (Fig. S5†). Initially, a mass increase appears at about 200 °C due to oxidation of small-sized silicon nanoparticles. Note that conventional silicon nanoparticles ranging from 50–150 nm are stable up to temperatures of about 800 °C due to a native SiO_2 layer and show no mass increase for an oxidation reaction.[13] However, the small-sized silicon nanoparticles (5 nm) at hand exhibit elevated reactivity due to their large surface area and hydride termination on the surface.[18] Hence, they are prone to oxidation in air even at temperatures far below 800 °C resulting in a mass gain already at about 200 °C. It is followed by a sudden mass

Table 1 Composition of silicon (wt%) within the polysiloxane after thermal processing at 1150 °C (in argon at 50 K min^{-1}) determined through EDXS, ^{29}Si MAS NMR and XPS

	HTCS	HDCS
Theoretically[a]	12.0	15.4
EDXS	13.7	21.2
NMR	9.0	10.4
XPS	5.6	6.0

[a] Considering the weight loss (3.5% for HTCS and 5.5% for HDCS) and a composition of ($HSiO_{1.5}$) for HTCS and $([H_2SiO]_1[HSiO_{1.5}]_{1.9}[SiO_2]_{0.15})_n$ for HDCS.

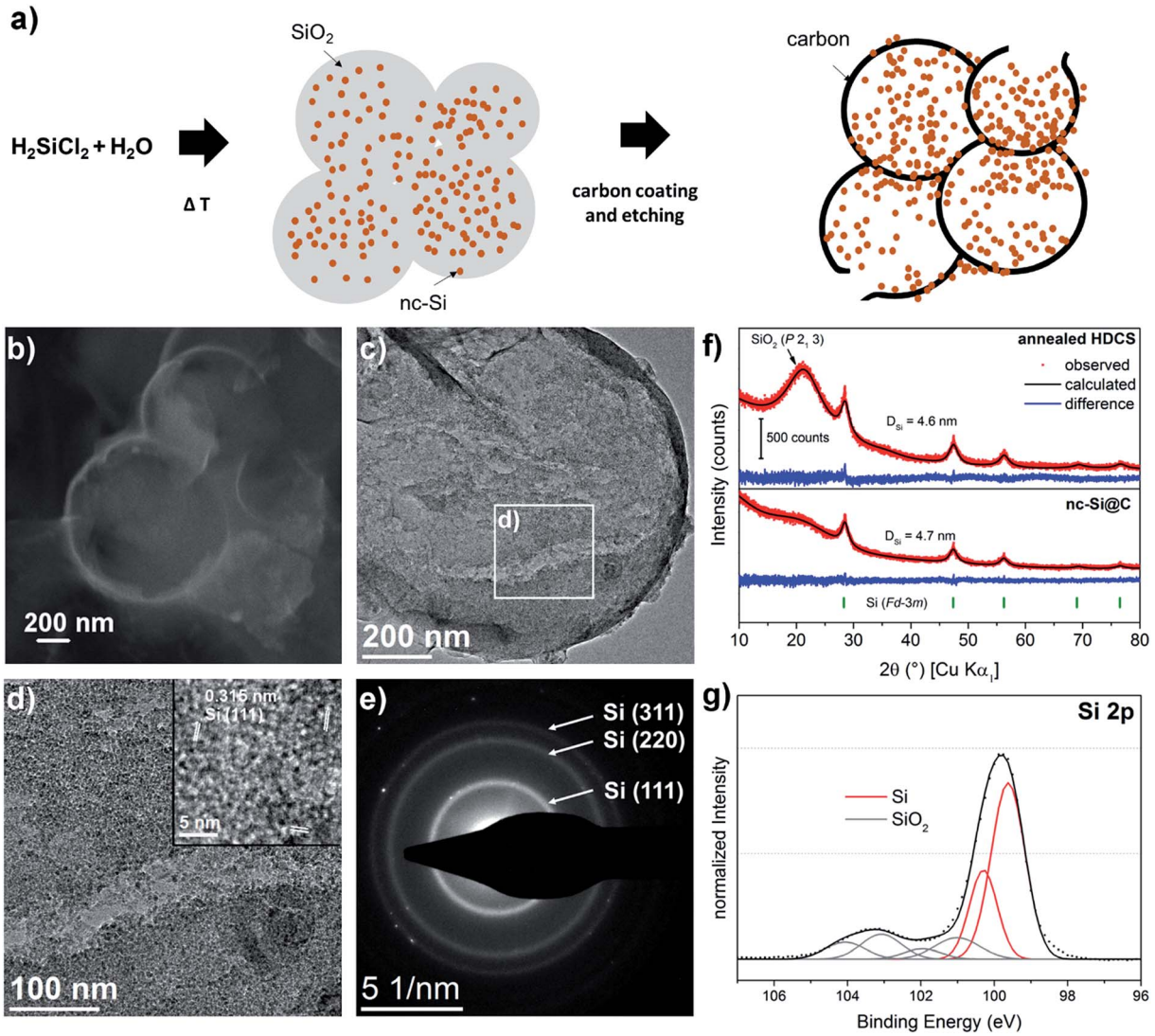

Fig. 3 (a) Schematic scheme of the annealed HDCS (left) and the final nc-Si@HCS (right), (b) SEM and (c) TEM bright-field images of nc-Si@HCS, (d) a high-resolution image proving the presence of silicon nanocrystallites with an average size of 5 nm and (e) the corresponding SAED pattern. (f) Observed and calculated XRD patterns of the annealed HDCS and nc-Si@HCS and (g) the XP spectrum of the Si 2p level of the as-prepared electrode composed of nc-Si@HCS.

loss of 15% at about 500 °C as a result of CO/CO_2 formation. Since the carbon oxidation process goes along with silicon oxidation, it cannot be concluded that the composite is composed of 15 wt% carbon and therewith 85 wt% silicon. Instead, a more reliable value is determined from the residual after combustion at 900 °C which is assumed to consist of pure SiO_2.[30] We determined a silicon content of 53 wt% which matches well with the EDXS results. However, a continued mass increase at 900 °C indicates incomplete oxidation and therewith incomplete silicon combustion. Hence, the silicon content may in fact be little higher than 53 wt%. Considering the employed sucrose to form the carbon and the silicon content of 22 wt% from the mass loss of HDCS after annealing, the theoretical silicon composition should be somewhere in the range of 75 wt% within the nc-Si@HCS indicating that the etching procedure partially dissolves very small silicon nanoparticles. Hence, there is further potential to increase the yield of silicon for example by adjusting the etching time and conditions. We examined individual carbon spheres by SEM and TEM. A representative SEM image of a typically retained carbon sphere is shown in Fig. 3b. As already indicated, in contrast, the sphere is hollow with large void space. The specific surface area and pore size distribution are determined by nitrogen physisorption measurements. A hysteresis loop is observed of the type H3 (ref. 31) due to pore condensation indicating a network of meso- and macropores with a moderate total volume of 0.25 $cm^3\ g^{-1}$ and a specific surface area of 313 $m^2\ g^{-1}$ (Fig. S6†). In Fig. 3c, a TEM image of such a sphere is depicted confirming the conclusions from the SEM analysis. Already at 12 000-fold magnification, finely dispersed particles inside the hollow carbon sphere are visible. Higher resolution (Fig. 3d) impressively reveals that indeed high quantities of silicon nanoparticles of about 5 nm in

average size inside the HCS are formed during synthesis. A high-resolution image shows several crystalline areas with a d-spacing of about 0.32 nm attributed to the (111) plane of cubic silicon with space group $Fd\bar{3}m$. Additional SAED patterns of the inset area in Fig. 3e clearly prove the presence of crystalline Si nanoparticles.

The XRD pattern (Fig. 3f) of the annealed HDCS shows two phases. The broad event at 22° 2θ is related to almost amorphous silica (space group $P2_13$). The other reflections at 28.5°,47.4°, 56.4°, 69.3°, 76.6° and 88.4° 2θ are assigned to the cubic structure of silicon (space group $Fd\bar{3}m$). The lattice parameter of the silicon was determined to be 5.4139(7) Å by a Rietveld analysis. By applying the Scherrer equation, a crystallite size of about 5 nm is determined, clearly proving the successful formation of silicon nanocrystallites. No other crystalline phases are observed. After etching in diluted HF to form the nc-Si@HCS anode material, the silica content significantly decreased as expected which is indicated by the almost diminished reflection intensity at about 22° 2θ, whereas the nanocrystalline silicon is mostly retained. The lattice constant of silicon slightly increased to 5.4198(6) Å probably as a result of less compression after the removal of the silica matrix. We still determined a crystallite size of about 5 nm for the silicon phase indicating that the silicon is rarely attacked by HF during the etching procedure. However, partial dissolution of very small silicon nanoparticles probably happens together with the silica dissolution. The as-prepared electrode composed of nc-Si@HCS was examined by XPS in order to determine the surface characteristics of silicon within the final electrode material. Note that the electrode includes 85 wt% of nc-Si@HCS and 15 wt% of binder and conductive carbon. The determined concentration of silicon atoms accounts to 22 wt%. The binding energy maximum in the Si 2p level (Fig. 3g) at 99.5 eV indicates that most of the surface silicon is in the elemental state since the integrated area accounts to 74%. Some surface oxidation of the silicon nanocrystallites is detected at binding energies above 101 eV. The level of oxidation accounts to 26% of the integrated area within the Si 2p spectrum which lies in the range of bulk silicon and is lower than typically observed for nanostructured silicon electrodes.[32] This observation impressively demonstrates that hydride-terminated silicon nanoparticles of 5 nm in size are stable in air and can be further processed under ambient conditions without significant oxidation. Interestingly, the silicon concentration determined by XPS (22 wt%) is much lower than the bulk composition of the electrode mixture which was determined by EDXS/TGA to be about 43 wt% silicon. The reason for the deviation is that most silicon nanocrystallites are located within the hollow carbon spheres and are therefore not detectable by the surface-sensitive XPS technique with an information depth of about 5 nm. Based on the XPS results, less than half of the silicon seems to be either attached to the outer shell of the carbon or embedded within half-open HCS. However, a careful examination of more TEM images (Fig. 3c) supports that the silicon nanocrystallites are more concentrated in the inner hollow carbon sphere than at the outer wall surface. We believe that our synthesis approach is an economical way to prepare large quantities of silicon nanocrystallites embedded inside hollow carbon structures, but needs further fine-tuning of the carbon coating to form a more homogeneous layer on the annealed HDCS.

Electrochemical characterization of nc-Si@HCS

All electrochemical tests were performed *versus* lithium metal in a commercial electrolyte typically used for LIBs (LP30). Cyclic voltammetry was carried out to identify the redox pairs in our electrode material and the results are presented in Fig. 4a. In the first lithiation process, a broad reduction current signal appears extending from 1 V to 0.3 V *vs.* Li/Li^+, which is attributed to SEI formation. At potentials lower than 0.1 V *vs.* Li/Li^+, a strong current is measured as a result of the amorphization of the crystalline silicon nanoparticles. During oxidation (delithiation), two signals with maxima at 0.326 mV and 493 mV *vs.* Li/Li^+ occur. Both signals are well known for the delithiation of Li_xSi alloys and grow with increasing cycle number as a result of incomplete lithiation in the first cycle. This activation process is very typical of nanostructured silicon anodes.[8,33] In the following cycles, an additional reduction signal with a maximum at 189 mV *vs.* Li/Li^+ appears which is also often observed for lithiation of amorphous silicon.[34] Overall, the results show that silicon is present as an active material for lithium storage.

The electrochemical performance for practical applications was tested by galvanostatic cycling between 0.01 and 1.2 V *vs.* Li/Li^+ at different current rates. Fig. 4b presents the galvanostatic discharge/charge curves at $I = 250$ mA g^{-1}. The first current is consumed at roughly 1.1 V *vs.* Li/Li^+ visible as an increasing slope of the cell potential *versus* capacity. The steep slope extends to about 0.1 V *vs.* Li/Li^+ mainly attributed to electrolyte decomposition and SEI formation as already observed by CV.[32] At a potential of about 0.08 V *vs.* Li/Li^+ a flat plateau appears as a result of transformation of the nanocrystalline silicon into amorphous Li_xSi. This plateau is very typical of a two-phase reaction. When the potential falls below 0.050 V *vs.* Li/Li^+ the crystalline $Li_{15}Si_4$ phase may be formed.[35] The delithiation curve shows a gradual increase of the voltage due to the reaction of amorphous Li_xSi to amorphous silicon. The average delithiation potential is at 0.45 V *vs.* Li/Li^+ which is highly favorable for negative electrode materials in LIBs. The initial coulombic efficiency is 69% and lies in the range of nanostructured silicon anodes.[10,36] The second discharge curve differs from the first one, as expected, because all crystalline particles have changed into an amorphous state after the first cycle.[37] Since there is no visible two-phase transition (crystalline-to-amorphous) anymore, the discharge voltage curve appears gradually decreasing with the continued current rate. The cycling stability is shown in Fig. 4c. Initially, a delithiation capacity of *ca.* 1560 mA h $g_{electrode}^{-1}$ is reached corresponding to about 3400 mA h $g_{silicon}^{-1}$. This capacity is four times higher than that observed for conventional graphite in LIBs. We compared the specific capacity to those of other HSQ derived anode materials recently reported in the literature. Our previously developed trichlorosilane-derived nc-Si@HCS shows a specific capacity of 1280 mA h $g_{electrode}^{-1}$ which is about 22% lower than that reported

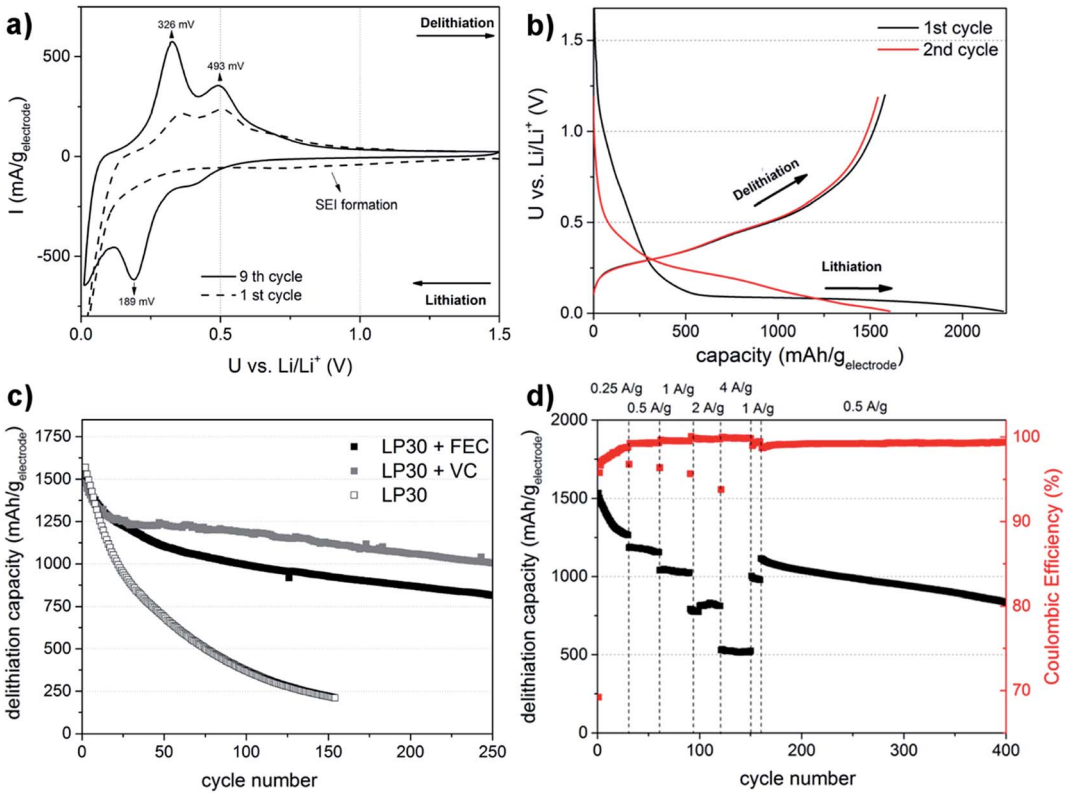

Fig. 4 (a) Cyclic voltammograms, (b) the first two discharge/charge voltage profiles of the nc-Si@HCS electrode in LP30 at $I = 250$ mA g^{-1}, (c) galvanostatic cycling of nc-Si@HCS at 250 mA g^{-1} in dependency of the addition of VC and FEC to the LP30 electrolyte and (d) galvanostatic cycling at different current rates in LP30 with FEC.

herein.[22] Bae *et al.* obtained about 960 mA h $g_{electrode}^{-1}$ at 200 mA g^{-1} using a hydrolyzed triethoxysilane-derived silicon anode.[17] Song *et al.* demonstrated 996 mA h $g_{electrode}^{-1}$ at 400 mA g^{-1} using a similar preparation method.[7] These results clearly highlight the potential of HDCS as a precursor. However, the reversibility is relatively poor in the commercial electrolyte and drops to 370 mA h $g_{electrode}^{-1}$ after 100 cycles. This rapid decrease in capacity is mainly attributed to a repeatedly growing SEI during cycling and indicates that the silicon nanocrystallites within the hollow carbon spheres are certainly covered with the electrolyte to form the SEI. Hence, the carbon spheres are permeable to the electrolyte. Other studies reported considerably higher reversibility with nanostructured silicon encapsulated within hollow carbon spheres than that observed for our material.[13,14,38] The superior reversibility may appear because of different electrolytes modified with additives such as fluoroethylene (FEC) and vinylene carbonate (VC), in order to stabilize the SEI on the nano-silicon and therewith to enhance the electrochemical reversibility. Both VC and FEC are the most frequently reported additives[39–42] and are often applied along with silicon anodes in various concentrations of up to 20 vol% to enhance the electrochemical performance.[10,13,14,38,43,44] In order to provide an appropriate comparison to other studies, we show the results with and without these additives. For both compounds, the electrochemical reversibility is drastically enhanced. With FEC, the capacity after 100 cycles accounts to 990 mA h $g_{electrode}^{-1}$ and with VC the retained capacity is even higher and accounts to 1200 mA h $g_{electrode}^{-1}$. After 250 cycles in the electrolyte with FEC, the capacity still accounts to 810 mA h $g_{electrode}^{-1}$ with a total capacity retention of 52%. Considering the VC electrolyte, a high capacity of 1000 mA h $g_{electrode}^{-1}$ is still maintained with a notable capacity retention of 65% which is three times greater than for commonly used graphite anodes even after 250 deep discharge cycles. Besides these very impressive values, the results also confirm our recent observations that VC outperforms FEC in terms of reversibility on silicon anodes for LIBs.[22] Different current rates were tested with FEC in the electrolyte (Fig. 4d) since FEC was found to be superior for high power applications. Even after 4 A g^{-1} the capacity still accounts to 500 mA h $g_{electrode}^{-1}$, which is around 40% higher than for commercially available graphite. After 400 cycles at different current rates the capacity still accounts to 820 mA h $g_{electrode}^{-1}$ accounting to a capacity retention of about 54%.

Our novel electrode material is also tested for its behaviour at high mass loadings to especially evaluate the practical relevance. The results are depicted in Fig. 5 and show that with only 3.2 mg cm^{-2}, an areal capacity of 4 mA h cm^{-2} equating to 1240 mA h g^{-1} is reached which fulfills one requirement for practical application in commercial LIBs. For comparison, a graphite anode typically needs an active mass of 12 mg cm^{-2} in order to achieve 4 mA h cm^{-2}. Herein, only 27% of the graphite mass is necessary to accomplish practical areal capacities, which implies

a considerable reduction of weight at the cellular level. After 50 cycles, the cell still provides an outstanding areal capacity of around 3 mA h cm^{-2}. Further improvements of cycle stability may be achieved with an optimized electrolyte configuration. The results are comparable to the literature. For example, Liu *et al.* demonstrated 100 cycles at 3 mA h cm^{-2} and a mass loading of 3.12 mg cm^{-2} with a hollow silico-carbon nanocomposite.[14] In comparison to the work of Liu *et al.*, we obtain similar results through a low-cost and highly interesting synthesis strategy.

Post-mortem TEM investigations were performed in order to investigate the structural integrity of the HCS with embedded silicon nanoparticles before and after electrochemical cycling. We chose the sample cycled with the VC additive as it offered the highest reversibility. A representative bright-field image is shown in Fig. 6a. For a better visualization, we also used the STEM mode with a high-angle annular dark-field (HAADF) detector (Fig. 6b) which demonstrates that the overall hollow carbon structure is retained proving the efficient design of the carbon cage to keep the silicon nanoparticles in good electrical contact over the period of cycling. The analyzed area contains silicon (9 wt%) originating from the active species as determined by EDXS (Fig. 6c). Additionally, high concentrations of carbon (55 wt%) and oxygen (35 wt%) are detected mostly as a result of electrolyte decomposition products from the electrolyte components ethylene carbonate, dimethyl carbonate and vinylene carbonate to form the SEI film. Interestingly, nearly no fluorine (<1 wt%) is observed implying almost no $LiPF_6$ decomposition. These results indicate a stabilized SEI preventing decomposition of the conductive salt and, therewith, again supports recent conclusion on the inactivity of LiF a SEI component.[22] Overall, the results demonstrate the well-working design of our electrode material.

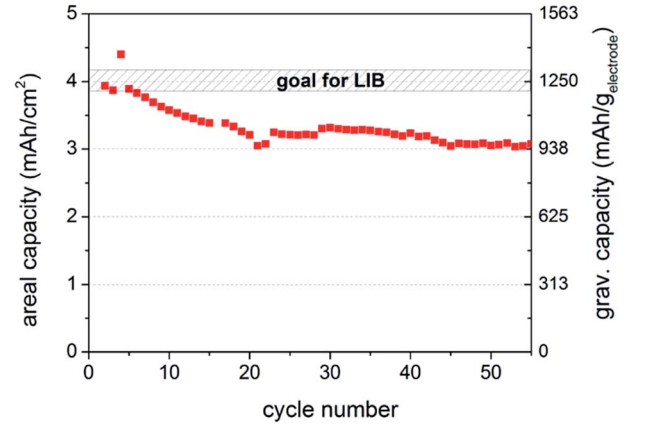

Fig. 5 Galvanostatic cycling of the nc-Si@HCS anode at 0.5 mA cm^{-2} for a mass loading of 3.2 mg cm^{-2} with the electrolyte LP30 with FEC addition.

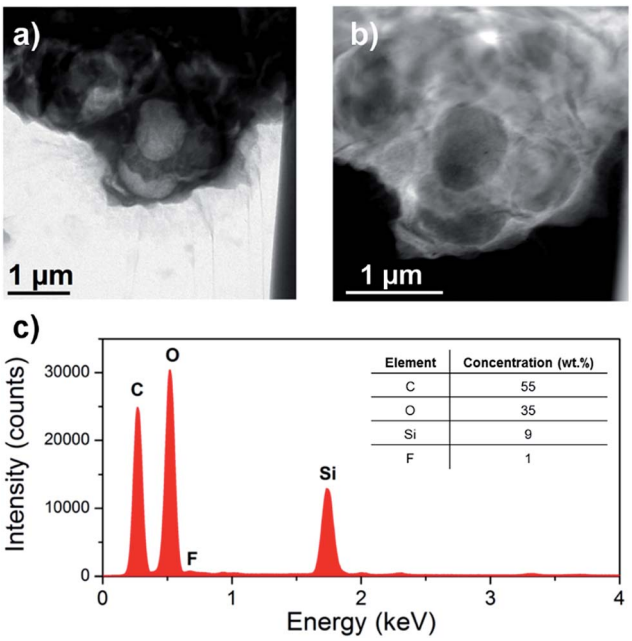

Fig. 6 *Post mortem* TEM of the nc-Si@HCS after 330 galvanostatic cycles in LP30 with VC. (a) Bright-field image, (b) HAADF image (STEM mode) and (c) EDX spectrum of the corresponding position.

Conclusion

We provide a novel and facile synthesis strategy based on a hydrogen-rich polysiloxane to obtain high quantities of silicon nanocrystallites embedded within spherical hollow carbon structures. Widely available dichlorosilane was used as feedstock and further processed through hydrolysis, temperature annealing at 1150 °C, carbon coating and etching, requiring no expensive or complex equipment. We obtained a considerably higher yield of silicon nanoparticles using a thermal processed HDCS instead of a hydrogen silsesquioxane typically derived from triethoxy- or trichlorosilane. The fabricated electrodes out of the final material were tested in LIBs and provide high specific capacities of up to 1580 mA h $g_{electrode}^{-1}$. Excellent reversibilities in commonly used electrolytes with FEC or VC addition for LIBs were demonstrated. A high areal capacity of 4 mA h cm^{-2} for an electrode with only 3.2 mg cm^{-2} electrode mass was demonstrated indicating that HDCS-derived anode materials are good candidates for practical application in LIBs. Post-mortem investigation reveals that the design of the carbon shell is retained over cycling which is an important feature for high reversibility. This study opens up new strategies to develop advanced anode materials for LIBs based on low-cost polysiloxanes with high potential for large-scale production.

Experimental

Synthesis of the nc-Si@HCS composite derived from HDCS and HTCS

The HDCS was prepared under an argon atmosphere using standard Schlenk techniques. 5.4 ml of deionized water (280 mmol) were added to 30 ml of a 40 wt% solution of H_2SiCl_2 (140 mmol) in toluene under vigorous stirring while cooling in an ice/water bath. After further stirring for 30 minutes the mixtures were heated up to 50 °C for one hour. After a few minutes of heating a white precipitate is formed. The solid was separated by filtration and dried under reduced pressure for several hours. Yield: 3.6 g (56 wt%). ^{29}Si MAS NMR data of HCDS: δ [ppm] =

−47.0 to −53.0 [H_2SiO]; −79.0 to −88.0 [$HSiO_{1.5}$]; −105.0 to −115.0 [SiO_2]. For the HTCS synthesis, we followed the standard procedure of our recent publication.[22]

1.5 g of the HDCS precursor was placed in a graphite crucible, if not otherwise mentioned, and annealed at 1150 °C ± 20 °C for 2 h under an argon atmosphere in an infrared oven (Gero LHTG 150-200/30-1G). The heating rate was about 50 K min^{-1} to a temperature of 800 °C and 12.5 K min^{-1} up to 1150 °C. During heating, traces of silane may evaporate out of the HDCS and deposit as silicon particles on the hot reactor wall. Afterwards the annealed and ground HDCS composite was wrapped into carbon. Then, 150 mg of sucrose were mixed with 1.5 g of the annealed HDCS and 4 ml of 3 wt% H_2SO_4 in a round-bottom flask with a magnetic stirrer. The solution was sonicated for 1 h and heated to 100 °C under vigorous stirring. After evaporation of water, the composite was dried at 150 °C overnight. The sucrose coating procedure was repeated once again. The material was then transferred into a Schlenk oven where it was carbonized at 900 °C (5 °C min^{-1}) for 5 h under an argon atmosphere. Finally, the carbonized material was etched with diluted HF. The material was transferred into a Teflon beaker with a magnetic stirrer. 10 ml of deionized water and 5 ml HCl (37 wt%, Merck KGaA) were added. Under vigorous stirring 10 ml of HF (40 wt%, Merck KGaA) were slowly dropped into the solution. The mixture was stirred for 30 min. in total and filtered twice with 40 ml water and 20 ml ethanol. The composite was dried under vacuum and stored under argon.

Electrode preparation

A slurry composed of nc-Si@HCS, Super P (Timcal) and poly-(acrylic acid) (PAA, Sigma-Aldrich) at a ratio of 85 : 10 : 5 was prepared with ethanol as the solvent for electrode fabrication. The slurry was homogenized for 15 min in a swing mill. The slurry was then coated on copper foil (MTI Corp. 25 μm thickness) with a blade coater (250 μm thickness) and dried for 30 min in air. 12 mm electrodes were punched out and stored under an argon atmosphere. Due to issues in the structural integrity of the electrodes at high mass loading (peeling off material from the copper foil), a cellular copper mesh[22] was infiltrated to demonstrate possible high areal capacity. All electrodes were dried at 100 °C under vacuum for at least 4 h prior to cell assembly. The electrode mass was determined by using a microbalance (Mettler Toledo XSE). Swagelok cells were assembled under an argon atmosphere (H_2O < 1 ppm, O_2 < 0.1 ppm). Two layers of a glass fiber (Whatman) were used as separators. We used 250 μl of 1 M $LiPF_6$ in EC/DMC (1 : 1 v/v) (LP30 Selectilyte, BASF) as the standard electrolyte, if not identified otherwise. The electrolyte additives fluoroethylene carbonate (Sigma-Aldrich, 99.9%, battery grade) and vinylene carbonate (Sigma-Aldrich, 99.9%, battery grade) were added in fractions of 20 vol% and 10 vol%, respectively, which turned out to be the optimized configuration.[22] Lithium metal (250 μm thickness, Chempur) was used as the counter electrode. For cyclic voltammetry (CV), a VMP3 system (Biologic) was used with a scan rate of 0.05 mV s^{-1} in the range of 0.01–1.5 V *vs.* Li/Li^+. A BaSyTec CTS was applied for galvanostatic cycling in the range of 0.01–1.2 V *vs.* Li/Li^+. The current rates ranging from 0.25 to 4 A g^{-1} were based on the mass of nc-Si@HCS and the capacities were calculated on the entire electrode mass (excluding copper). All measurements were recorded at 25 °C in a climate chamber.

Materials characterization

Fourier transform infrared (FTIR) spectroscopy was carried out on a Thermo Scientific Nicolet 6700 spectrometer in attenuated total reflection (ATR) mode between 600 and 3000 cm^{-1}. The spectra were normalized to 1. ^{29}Si solid state NMR measurements were performed at 79.51 MHz on a Bruker AVANCE III HD 400 MHz WB spectrometer using 7 mm ZrO_2 rotors and a DVT/MAS probe. For single pulse experiments, 30° pulses were applied at experiment recycle delays of 60 s. Tppm15 decoupling was applied. The chemical shift was referenced using the high-field signal of the Q^4-groups in Q_8M_8 (octakis-(trimethylsiloxy)silsesquioxane: −109 ppm with respect to TMS = 0 ppm). For X-ray powder diffraction (XRD), a STOE Stadi P diffractometer with a curved Ge(111) crystal monochromator and a 6°-position sensitive detector was used. The as-synthesized powder was pressed between acetate foils and fixed with a collodion glue. The samples were measured in the range of $10° \leq 2\theta \leq 90°$ with a step size of $\Delta 2\theta = 0.01°$ in transmission geometry with Cu $K_{\alpha 1}$ radiation. Rietveld analysis was performed with the program MAUD.[45] For scanning electron microscopy (SEM) a LEO Gemini 1530 microscope was used. The acceleration voltage was set to 10 kV and a Bruker detector (XFlash 6) was employed for energy-dispersive X-ray spectroscopic (EDXS) analysis. For transmission electron microscopy (TEM), a FEI Tecnai F30 with a field emission gun and 300 kV acceleration voltage equipped with a EDXS detector was applied. Thermogravimetric analysis in synthetic air was conducted with a Netzsch Jupiter STA 449C. For nitrogen sorption experiments, a Quantachrome Quadrasorb SI apparatus was used. The sample was degassed under dynamic vacuum at 423 K overnight before carrying out sorption experiment. Specific surface areas were calculated at a relative pressure $p/p0 = 0.05$–0.3 using the multi point Brunauer–Emmett–Teller (BET) method. The total pore volume was calculated at $p/p0 = 0.89$. For post-mortem investigation, the cell was cycled 330 times at $I = 250$ mA g^{-1} between 0.01 and 1.2 V *vs.* Li/Li^+ in LP30 with VC and disassembled in the delithiated state inside a glovebox under an inert atmosphere (H_2O < 1 ppm, O_2 < 0.1 ppm). The electrode material was dispersed in 2 ml DMC by sonication and dropped onto a copper grid with a lacey carbon film for TEM investigation. During transfer into the TEM, the sample was exposed to air for about 1 min. X-ray photoemission spectroscopy (XPS) was carried out with a Physical Electronics PHI 5600 CI system with Mg K_α (1253.6 eV) radiation at 350 W with a pass energy of 29 eV and a step size of 0.1 eV. The binding energies were used without further referencing. Elemental concentrations from the XP spectra were calculated using standard single-element sensitivity factors. The core level signals were fitted with a Gaussian function using a basic linear background after normalization to 1.

Acknowledgements

The authors thank Silke Hampel and Alexander Schubert for their valuable technical support and Cornelia Geringswald for thermogravimetric analysis. Stefanie Kaschube is gratefully acknowledged for the XPS measurements. Martin Uhlemann is thanked for carrying out the nitrogen sorption measurement. Parts of this work are funded by the German Federal Ministry of Research and Education (BMBF) within the ExcellentBattery program realized by the WING center "BamoSa – Battery mobility in Saxony" (grant no. 03X4637).

References

1 D. Larcher and J.-M. Tarascon, *Nat. Chem.*, 2015, **77**, 19–29.
2 P. G. Bruce, S. A. Freunberger, L. J. Hardwick and J.-M. Tarascon, *Nat. Mater.*, 2012, **11**, 19–30.
3 C.-M. Park, J.-H. Kim, H. Kim and H.-J. Sohn, *Chem. Soc. Rev.*, 2010, **39**, 3115–3141.
4 X. H. Liu, L. Zhong, S. Huang, S. X. Mao, T. Zhu and J. Y. Huang, *ACS Nano*, 2012, **6**, 1522–1531.
5 S. W. Lee, M. T. McDowell, L. A. Berla, W. D. Nix and Y. Cui, *Proc. Natl. Acad. Sci. U. S. A.*, 2012, **109**, 4080–4085.
6 H. Kim, M. Seo, M.-H. Park and J. Cho, *Angew. Chem., Int. Ed.*, 2010, **49**, 2146–2149.
7 J. Song, S. Chen, M. Zhou, T. Xu, D. Lv, M. L. Gordin, T. Long, M. Melnyk and D. Wang, *J. Mater. Chem. A*, 2014, **2**, 1257–1262.
8 Y.-X. Yin, S. Xin, L.-J. Wan, C.-J. Li and Y.-G. Guo, *J. Phys. Chem. C*, 2011, **115**, 14148–14154.
9 X. Su, Q. Wu, J. Li, X. Xiao, A. Lott, W. Lu, B. W. Sheldon and J. Wu, *Adv. Energy Mater.*, 2014, **4**, 1300882.
10 H. Wu, G. Chan, J. W. Choi, I. Ryu, Y. Yao, M. T. McDowell, S. W. Lee, A. Jackson, Y. Yang, L. Hu and Y. Cui, *Nat. Nanotechnol.*, 2012, **7**, 310–315.
11 H. Wu and Y. Cui, *Nano Today*, 2012, **7**, 414–429.
12 Y.-M. Lin, K. C. Klavetter, P. R. Abel, N. C. Davy, J. L. Snider, A. Heller and C. B. Mullins, *Chem. Commun.*, 2012, **48**, 7268–7270.
13 N. Liu, Z. Lu, J. Zhao, M. T. McDowell, H.-W. Lee, W. Zhao and Y. Cui, *Nat. Nanotechnol.*, 2014, **9**, 187–192.
14 N. Liu, H. Wu, M. T. McDowell, Y. Yao, C. Wang and Y. Cui, *Nano Lett.*, 2012, **12**, 3315–3321.
15 S.-K. Lee, S.-M. Oh, E. Park, B. Scrosati, J. Hassoun, M.-S. Park, Y.-J. Kim, H. Kim, I. Belharouak and Y.-K. Sun, *Nano Lett.*, 2015, **15**, 2863–2868.
16 T. Jaumann, M. Herklotz, M. Klose, K. Pinkert, S. Oswald, J. Eckert and L. Giebeler, *Chem. Mater.*, 2015, **27**, 37–43.
17 J. Bae, D. S. Kim, H. Yoo, E. Park, Y.-G. Lim, M.-S. Park, Y.-J. Kim and H. Kim, *ACS Appl. Mater. Interfaces*, 2016, **8**, 4541–4547.
18 C. M. Hessel, E. J. Hendersson and J. G. C. Veinot, *Chem. Mater.*, 2006, **18**, 6139–6146.
19 E. J. Henderson, J. A. Kelly and J. G. C. Veinot, *Chem. Mater.*, 2009, **21**, 5426–5434.
20 Z. Lu, N. Liu, H.-W. Lee, J. Zhao, W. Li, Y. Li and Y. Cui, *ACS Nano*, 2015, **9**, 2540–2547.
21 M. Pauthe, E. Bernstein, J. Dumas, L. Saviot, A. Pradel and M. Ribes, *J. Mater. Chem.*, 1999, **9**, 187–191.
22 T. Jaumann, J. Balach, U. Langklotz, V. Sauchuk, M. Fritsch, A. Michaelis, V. Teltevskij, D. Mikhailova, S. Oswald, M. Klose, G. Stephani, R. Hauser, J. Eckert and L. Giebeler, *Energy Storage Mater.*, 2017, **6**, 26–35.
23 D. Seyferth, C. Prud'homme and G. H. Wiseman, *Inorg. Chem.*, 1983, **22**, 2163–2167.
24 M. Cypryk and Y. Apeloig, *Organometallics*, 1997, **16**, 5938–5949.
25 P. A. Agaskar and W. G. Klemperer, *Inorg. Chim. Acta*, 1995, **229**, 355–364.
26 R. Riedel, E. Kroke, A. Greiner, A. O. Gabriel, L. Ruwisch, J. Nicolich and P. Kroll, *Chem. Mater.*, 1998, **10**, 2964–2979.
27 G. Engelhardt and H. Jancke, *Polym. Bull.*, 1981, **5**, 577–584.
28 G. W. Fester, J. Wagler, E. Brendler, U. Böhme, G. Roewer and E. Kroke, *Chem.–Eur. J.*, 2008, **14**, 3164–3176.
29 G. W. Fester, J. Wagler, E. Brendler, U. Böhme, D. Gerlach and E. Kroke, *J. Am. Chem. Soc.*, 2009, **131**, 6855–6864.
30 A. M. Wilson and J. R. Dahn, *J. Electrochem. Soc.*, 1995, **142**, 326–332.
31 S. J. Gregg and K. S. W. Sing, *Adsorption, surface area and porosity*, Academic Press, New York, 1982.
32 B. Philippe, R. Dedryvére, J. Allouche, F. Lindgren, M. Gorgoi, H. Rensmo, D. Gonbeau and K. Edström, *Chem. Mater.*, 2012, **24**, 1107.
33 H. Wu, G. Yu, L. Pan, N. Liu, M. T. McDowell, Z. Bao and Y. Cui, *Nat. Commun.*, 2013, **4**, 1943.
34 E. Pollak, G. Salitra, V. Baranchugov and D. Aurbach, *J. Phys. Chem. C*, 2007, **111**, 11437–11444.
35 K. Ogata, E. Salager, C. J. Kerr, A. E. Fraser, C. Ducati, A. J. Morris, S. Hofmann and C. P. Grey, *Nat. Commun.*, 2014, **5**, 3217.
36 X. Liu, Y. Gao, R. Jinc, H. Luo, P. Peng and Y. Liu, *Nano Energy*, 2014, **4**, 31–38.
37 J. Li and J. R. Dahn, *J. Electrochem. Soc.*, 2007, **154**, A156–A161.
38 S. Chen, M. L. Gordin, R. Yi, G. Howlett, H. Sohn and D. Wang, *Phys. Chem. Chem. Phys.*, 2012, **14**, 12741–12745.
39 L. Leveau, B. Laik, J.-P. Pereira-Ramos, A. Gohier, P. Tran-Van and C.-S. Cojocaru, *Electrochim. Acta*, 2015, **157**, 218–224.
40 S. Dalavi, R. Guduru and B. L. Lucht, *J. Electrochem. Soc.*, 2012, **159**, A642–A646.
41 N.-S. Choi, K. H. Yew, K. Y. Lee, M. Sung, H. Kim and S.-S. Kim, *J. Power Sources*, 2006, **161**, 1254–1259.
42 L. Chen, K. Wang, X. Xie and J. Xiea, *Electrochem. Solid-State Lett.*, 2006, **9**, A512–A515.
43 M. Gauthier, D. Mazouzi, D. Reyter, B. Lestriez, P. Moreau, D. Guyomard and L. Rou, *Energy Environ. Sci.*, 2013, **6**, 2145.
44 Y.-S. Hu, R. Demir-Cakan, M.-M. Titirici, J.-O. Müller, R. Schlögl, M. Antonietti and J. Maier, *Angew. Chem., Int. Ed.*, 2008, **47**, 1645–1649.
45 L. Lutterotti, D. Chateigner, S. Ferrari and J. Ricote, *Thin Solid Films*, 2004, **450**, 34–41.